The endoplasmic reticulum contributes to lysosomal tubulation/sorting driven by LRRK2

Luis Bonet-Ponce●,* and Mark R. Cookson●,*
Cell Biology and Gene Expression Section, National Institute on Aging, National Institutes of Health, Bethesda, MD 20892

ABSTRACT Lysosomes are dynamic organelles that can remodel their membrane as an adaptive response to various cell signaling events including membrane damage. Recently, we have discovered that damaged lysosomes form and sort tubules into moving vesicles. We named this process LYTL for LYsosomal Tubulation/sorting driven by LRRK2, as the Parkinson's disease protein LRRK2 promotes tubulation by recruiting the motor adaptor protein JIP4 to lysosomes via phosphorylated RAB proteins. Here we use spinning-disk microscopy combined with superresolution to further characterize LYTL after membrane damage with LLOMe (L-leucyl-L-leucine methyl ester). We identified the endoplasmic reticulum (ER) colocalizing with sites of fission of lysosome-derived tubules. In addition, modifying the morphology of the ER by reducing ER tubules leads to a decrease in LYTL sorting, suggesting that contact with tubular ER is necessary for lysosomal membrane sorting. Given the central roles of LRRK2 and lysosomal biology in Parkinson's disease, these discoveries are likely relevant to disease pathology and highlight interactions between organelles in this model.

INTRODUCTION

Lysosomes are typically rounded organelles with degradative capacity that turn over macromolecules taken up via the endosomal system or intracellular organelles due to interactions with the autophagy machinery. They are dynamic structures that can also 1) act as signaling stations regulating the nutrient-sensing response (for a review, see Ballabio and Bonifacino, 2020), 2) promote mitochondrial division by establishing membrane contact sites (Wong *et al.*,

2018), 3) regulate free cholesterol transport to peroxisomes (Chu *et al.*, 2021) and the endoplasmic reticulum (ER) (Höglinger *et al.*, 2019; Lim *et al.*, 2019; Meng *et al.*, 2020), 4) remodel neuronal spines (Goo *et al.*, 2017; Padamsey *et al.*, 2017), and 5) cotransport mitochondria (Guo *et al.*, 2018), ER tubules (Spits *et al.*, 2021), or RNA granules (Liao *et al.*, 2019) via hitchhiking. These observations indicate that lysosomes play a central role in cellular homeostasis.

During the performance of these functions in the cell, the lysosomal membrane is prone to damage and it is now recognized that there are multiple mechanisms involved in lysosomal membrane repair and turnover (for a review, see Zoncu and Perera, 2022). When the damage is limited, lysosomes recruit ESCRT (endosomal sorting complexes required for transport) members to repair the membrane (Radulovic *et al.*, 2018; Skowyra *et al.*, 2018). If the damage persists, the cell initiates a clearance process of ruptured lysosomes through autophagy termed lysophagy (Maejima *et al.*, 2013). The recognition of exposed lysosomal luminal glycans by galectins initiates lysophagy (Maejima *et al.*, 2013; Jia *et al.*, 2018, 2020), followed by recruitment of the autophagy machinery (Chauhan *et al.*, 2016; Eapen *et al.*, 2021). We have recently shown that in addition to repair and lysophagy, lysosomal membrane damage also triggers a tubulation and membrane sorting process we named LYTL (LYsosomal Tubulation/sorting driven by LRRK2) (Bonet-Ponce *et al.*, 2020). LYTL is regulated by leucine-rich repeat kinase 2 (LRRK2). LRRK2 is a large protein with GTPase and kinase activity (Cookson, 2010) that is activated at membranes (Bonet-Ponce and Cookson, 2019, 2021)

and can phosphorylate a subset of RAB GTPases (Steger *et al.*, 2016). Upon lysosomal membrane damage, LRRK2 is recruited to damaged lysosomes and phosphorylates and brings RAB10 to the lysosomal membrane. In turn, pRAB10 recruits its effector JIP4 (C-jun-amino-terminal kinase-interacting protein 4, a motor adaptor protein) that promotes the formation of a lysosomal tubule negative for lysosomal membrane markers. The JIP4-positive LYTL tubule can be resolved into vesicles that travel through the cytosol and contact healthy lysosomes (Bonet-Ponce *et al.*, 2020). Nonetheless, little is known about the mechanisms underneath the elongation of the tubule and its subsequent sorting into moving vesicles. Gain-of-function mutations in *LRRK2* are a common monogenic cause of Parkinson's disease (PD), and noncoding variants at the LRRK2 locus increase risk of sporadic PD (Paisán-Ruíz *et al.*, 2004; Zimprich *et al.*, 2004; Nalls *et al.*, 2019). Lysosomes are critical organelles not only in PD pathobiology (Klein and Mazzulli, 2018) but also in several other neurodegenerative diseases (Udayar *et al.*, 2022). Interestingly, LRRK2 has recently been identified as a risk factor for progressive supranuclear palsy (Jabbari *et al.*, 2021). Thus, understanding lysosomes generally and LYTL specifically may provide insight into pathogenic events across multiple neurological disorders.

Here we use superresolution spinning-disk microscopy to capture the dynamic nature of LYTL with enhanced resolution and classify the JIP4-positive tubules into different subtypes. We found that even though LYTL tubules are highly dynamic, only a small proportion of them undergo membrane sorting. Furthermore, we detect the presence of ER tubules marking the sorting site, and modification of the ER morphology leads to a decrease in membrane sorting, indicating that contact with ER is necessary for lysosomal membrane fission before sorting in the context of LYTL.

RESULTS

Our prior description of LYTL used Airyscan imaging in fixed mouse primary astrocytes (Bonet-Ponce *et al.*, 2020). To formally demonstrate that LYTL can be induced in additional cells, we treated LRRK2 transfected U2OS cells with 1 mM LLOMe (ʟ-leucyl-ʟ-leucine methyl ester) for 2 h and immunostained for different markers. Using this approach, we identified multiple JIP4-positive tubules that are negative for the lysosomal membrane markers LAMP1, LAMP2, TMEM192, LAMTOR4, and ARL8B that remained segregated in the vesicular part of the lysosomes (Supplemental Figure S1, A–F). This separation of lysosomal markers after induction of tubulation was confirmed in mouse primary astrocytes (Supplemental Figure S2C) (Bonet-Ponce *et al.*, 2020). The distribution of different markers to the lysosome and tubule is not a consequence of aldehyde-based fixation as LAMP1 is also absent from the JIP4-positive tubules in live cells (Supplemental Figure S1A; Figure 1B). As expected, the LRRK2 substrate and JIP4 interactor pRAB10 colocalizes with JIP4 at LYTL tubules (Supplemental Figure S1E). The induction of LYTL is a response to lysosomal damage, as another lysosomotropic reagent (chloroquine, CQ) also triggers LRRK2 recruitment and JIP4 tubulation (Supplemental Figure S2, A and B).

Tubule types classified with spinning-disk superresolution microscopy

To further study LYTL, in the current study we used SoRa, a confocal microscope that combines spinning-disk with superresolution imaging to a maximum resolution of 120 nm after deconvolution (Azuma and Kei, 2015). This approach allowed us to explore LYTL as a dynamic process with enhanced resolution compared with conventional confocal microscopy, permitting a precise visualization of the JIP4-positive LYTL tubules (Figure 1A). The LYTL tubules in living

cells were heterogeneous, with lengths ranging between 0.481 and 13 µm (mean = 2.6 µm, SEM = 0.2662; Supplemental Figure S2. D and E). Furthermore, the tubules display various shapes (Figure 1, A–G; Supplemental Movie 1) and in some cases we noted different tubules coming from the same lysosome that were intertwined with each other (Figure 1, B–E; Supplemental Movie 1). LYTL tubules can also bifurcate, creating smaller subtubules that emanate from the original tubule (Figure 1, F and G).

Using time-lapse imaging over 4 min intervals, we classified the LYTL tubules into three main groups: Stable, Retractile, and Sorting. Retractile tubules are tubules that, after elongation, move back to the lysosomal membrane (Figure 2A; Supplemental Figure S4A; Supplemental Movie 2). Stable tubules are steady in length and shape and do not undergo membrane sorting, although they are shown to be dynamic (Figure 2B; Supplemental Movie 2). Retractile tubules generate an excess membrane when they reach the lysosomal membrane (Supplemental Figure S4A). Consequently the excess membrane can either dissolve into the lysosomal membrane (Supplemental Figure S4B) or move to be part of an existing tubule from the same lysosome (Supplemental Figure S4C). Alternatively, Retractile tubules can regrow in the same or different part of the lysosome and be sorted after rebudding (Supplemental Figure S4D). Of the three major types of tubules, membrane sorting tubules were the most dynamic as they can fission their membranes, resolving the tubules into moving vesicles (Figure 2C; Supplemental Movie 2). Membrane sorting tubules were therefore further grouped into three categories, depending on the sorting type: Type I, Type II, and Type III. Type I sorting occurs when the entire tubule (or almost) is sorted, leaving a noodle-shaped membrane moving in the cytosol (Figure 2C; Supplemental Movie 2). Notably, Type I fissioned tubules will undergo secondary processing after being released from lysosomes and will be further fissioned into small vesicles (Supplemental Figure S3; Supplemental Movie 3) away from their original lysosome. Type II sorting occurs when only the tip of a tubule is fissioned, forming a moving vesicle (Figure 2C; Supplemental Movie 2). Finally, we name Type III sorting when a small tubule, approximately the size of a vesicle, is directly released from the lysosomal membrane without the apparent formation of a LYTL tubule (Figure 2C; Supplemental Movie 2). Stable and Retractile tubules are the most frequent tubule types, with frequencies of 47.84 and 36.04%, respectively, while membrane sorting tubules represented only ~16% all LYTL tubules (Figure 2D). Among the Sorting tubules, Type I was the most frequent sorting type (63%), followed by Type II (24.58%), and finally Type III (only 10.86%) (Figure 2E). These results suggested that sorted tubules may have specific mechanism(s) by which fission occurs. We therefore considered whether interaction with other organelles might contribute to membrane sorting tubule fission. We have previously noted contacts between the ER and the JIP4-positive LYTL tubules using focused ion beam scanning electron microscopy (FIB-SEM; Bonet-Ponce *et al.*, 2020).

The ER is present at the constriction site before the tubule fission

The ER is a large dynamic organelle that occupies the cytosol of eukaryotic cells and has many functions to preserve cell homeostasis, namely protein translation, Ca^{2+} regulation, or protein transport and folding, among others (Araki and Nagata, 2011). The ER is also able to form contacts with other compartments (Valm *et al.*, 2017) that are essential to mediate membrane fission (Wu *et al.*, 2018) of mitochondria, early and late endosomes, and even in membrane-less compartments such as RNA granules. Thus we tested whether the ER could be involved in mediating lysosomal tubule fission.
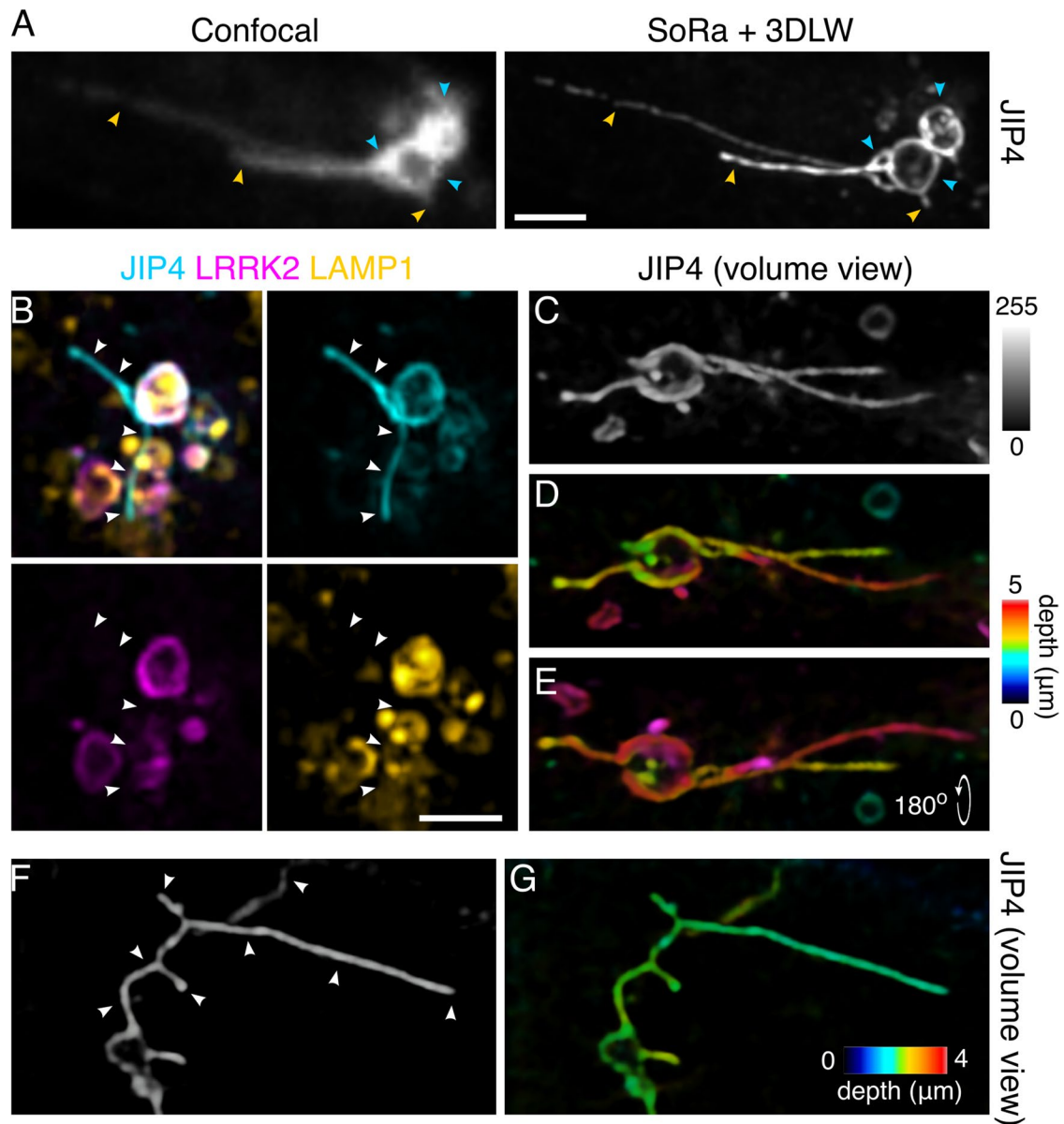
FIGURE 1: JIP4-positive tubules visualized using superresolution microscopy. (A) U2OS cells were transfected with 3xFLAG-LRRK2 and mNeonGreen-JIP4. After treatment with 1 mM LLOMe for 2 h, cells were fixed and observed with a confocal microscope. The image on the left was taken with conventional confocal settings while the image on the right was taken with SoRa and deconvolved using the 3D Landweber algorithm. (B) Cells transfected with mScarlet-LRRK2 (magenta), mNeonGreen-JIP4 (cyan), and LAMP1-HaloTag (yellow) were treated with LLOMe (1 mM, 2 h) and observed live with SoRa. Arrowheads show two JIP4-positive LYTL tubules that are also negative for LRRK2 and LAMP1. (C–E) Representative confocal picture of a live cell expressing 3xFLAG-LRRK2 and mNeonGreen-JIP4 (cyan). (C) Volume view of a lysosome with multiple tubules in gray, depth coded (D) and depth coded rotated 180° (E). (F, G) Volume view of a JIP4-positive lysosome displaying a bifurcated tubule in gray (white arrowheads; F) and depth color code (G). Blue arrowhead marks JIP4-positive lysosomes while yellow arrowheads show JIP4-positive tubules. Scale bar = 2 μm.

Live-cell imaging experiments, tracking tubules that undergo fission, reveal the presence of the ER in the tubule constriction site (Figure 3, A and B; Supplemental Figure S5, A–E; Supplemental Movie 4). We defined constriction site as the location where, in the frame before the tubule fission, the position of the JIP4-positive tubule where the fission will occur and has a decrease of fluorescence intensity (see line scans in Figure 3B; Supplemental Figure S5, B and E, and Figure 4C). The ER was fully present at the constriction site 65.9% of the time, while we see a partial presence of the ER 29.5% of the time and we did not detect the ER in a small minority of

instances (4.54%) (Figure 3C). When we examined the frequency of different sorting types that are associated with the ER, we observed similar percentages with ER (Figure 3D; Type I = 58.6%; Type II = 27.6%; Type III = 13.8%) compared with the overall sorting types (Type I = 63%; Type II = 26%; Type III = 11%) (Figure 2E), suggesting that the sorting type was independent of the ER. We were also able to observe the total presence of the ER during LYTL fission in mouse primary astrocytes (Figure 3E; Supplemental Figure S5F).

As we have previously shown (Kluss *et al.*, 2020, 2022), LRRK2 preferentially recruits JIP4 to perinuclear lysosomes. Consequently,
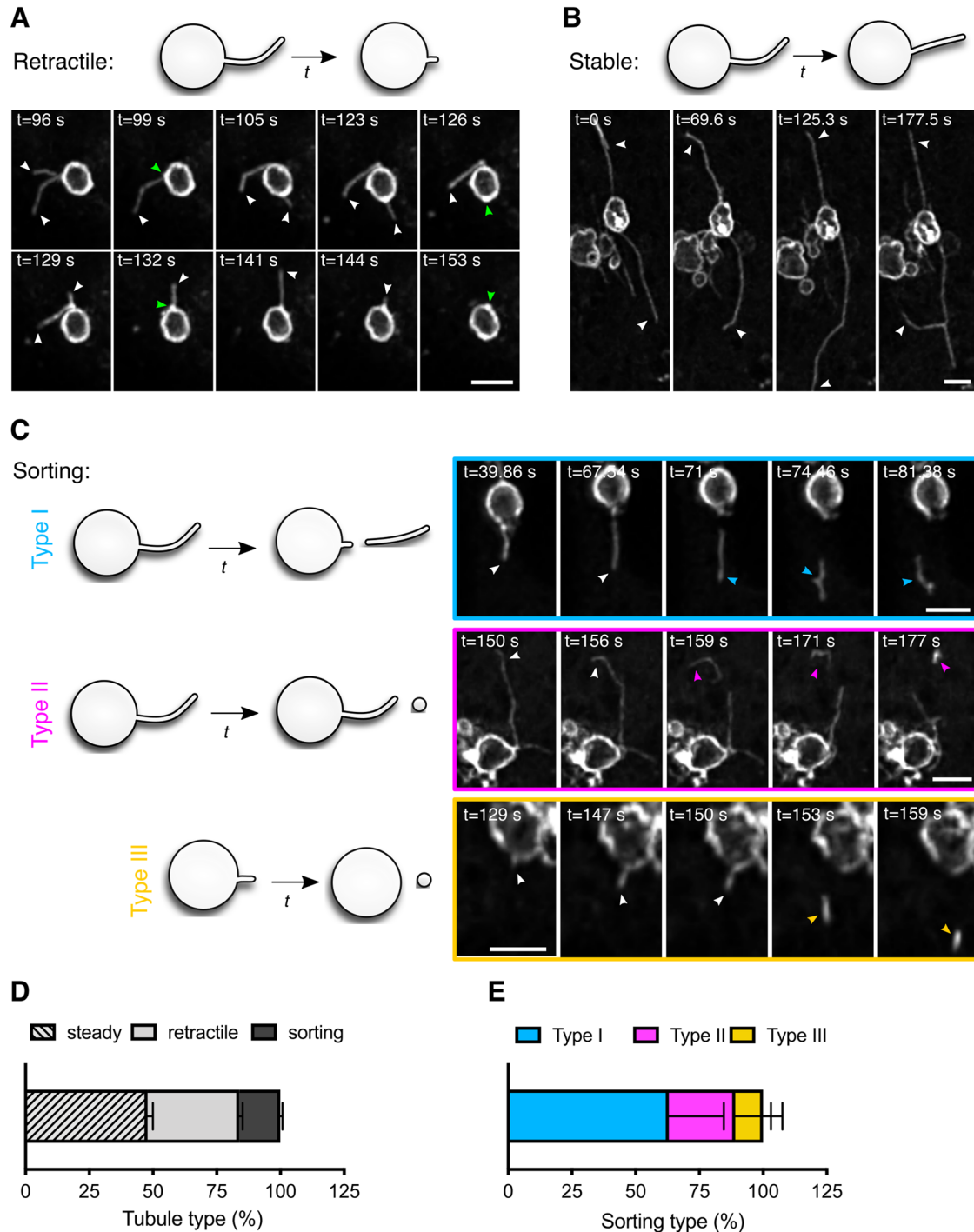
FIGURE 2: Classification of JIP4-positiveLYTL tubules. U2OS cells were transfected with 3xFLAG-LRRK2 and mNeonGreen-JIP4, treated with LLOMe (1 mM, 2 h), and imaged using a confocal microscope. (A) Representative time-lapse images of several Retractile LYTL tubules stemming from the same lysosome. (B) Representative time-lapse images of two Stable tubules budding from the same lysosome. (C) Representative time-lapse images of Type I sorting (top, blue), Type II sorting (middle, yellow), and Type III sorting (bottom, magenta) events. (D) Graph showing the frequency in percentage of the different tubule types. Data are mean ± SEM ($n = 2$ independent biological experiments). (E) Graph showing the frequency in percentage of the sorting types. Data are mean ± SEM ($n = 2$ independent biological experiments). White arrowheads indicate LYTL tubules and color arrowheads (blue, yellow, and magenta) signal sorting types with blue = Type I sorting, magenta = Type II sorting, and yellow = Type III sorting. Scale bar = 2 μm.

LYTL tubules are formed almost exclusively in the perinuclear area (Figure 4B), where the ER is densely packed, as opposed to the peripheral ER, which forms a clear and distinct monolayer (Figure 4A). Thus, to ensure that the colocalization of the ER at the constriction site is not a random event, we compared the fluorescence intensity of the ER at the constriction site in the original picture and after the ER has been rotated 90° to the right (Figure 4, C–E) to randomize its position. Our data show a significant decrease (1.7 fold) of the ER
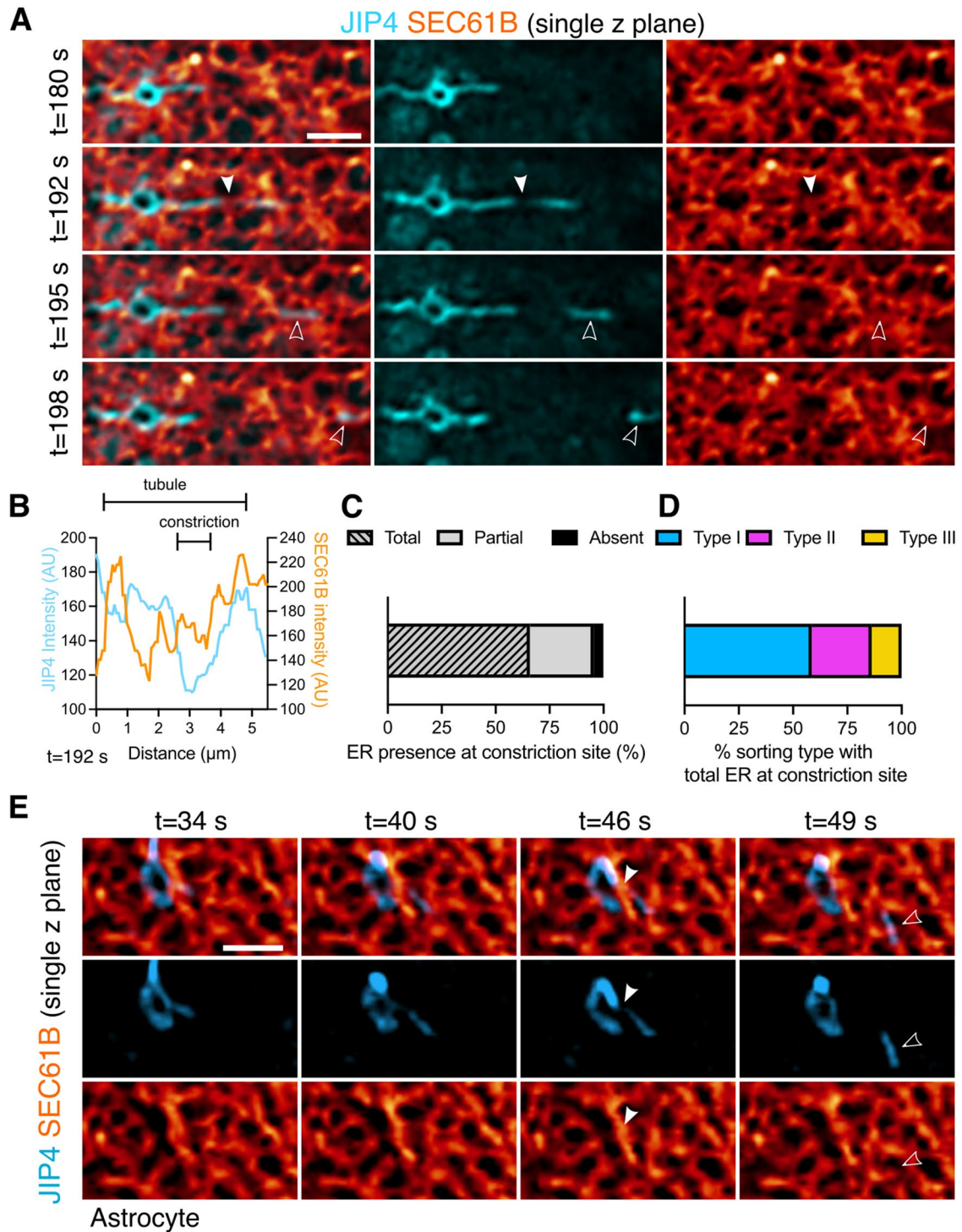
FIGURE 3: The ER is present at the LYTL tubule fission sites. (A) U2OS cells were transfected with 3xFLAG-LRRK2, HaloTag-JIP4 (cyan), and mNeonGreen-SEC61B (orange). Cells were treated with LLOMe (1 mM, 2 h) and visualized with a confocal microscope. Time-lapse imaging shows the presence of the ER at the tubule constriction site before the fission of the membrane. (B) Line scan along a LYTL tubule showing the fluorescence intensity of JIP4 and SEC61B at $t = 192$ s. (C) Graph shows the frequency of ER presence at the constriction site (in percentage) ($n = 44$ independent cells). (D) Graph shows the different sorting types among the ones that have a total presence of ER at the constriction site. (E) Mouse primary astrocytes were transfected with 3xFLAG-LRRK2 (G2019S), mNeonGreen-JIP4 (blue), and HaloTag-SEC61B (orange). Cells were treated with LLOMe (1 mM, 6 h) and observed under a confocal microscope. White arrowheads signal the constriction site. Outlined arrowheads indicate the sorted product. Pictures are shown in one single z plane. Scale bar = 2 μm.
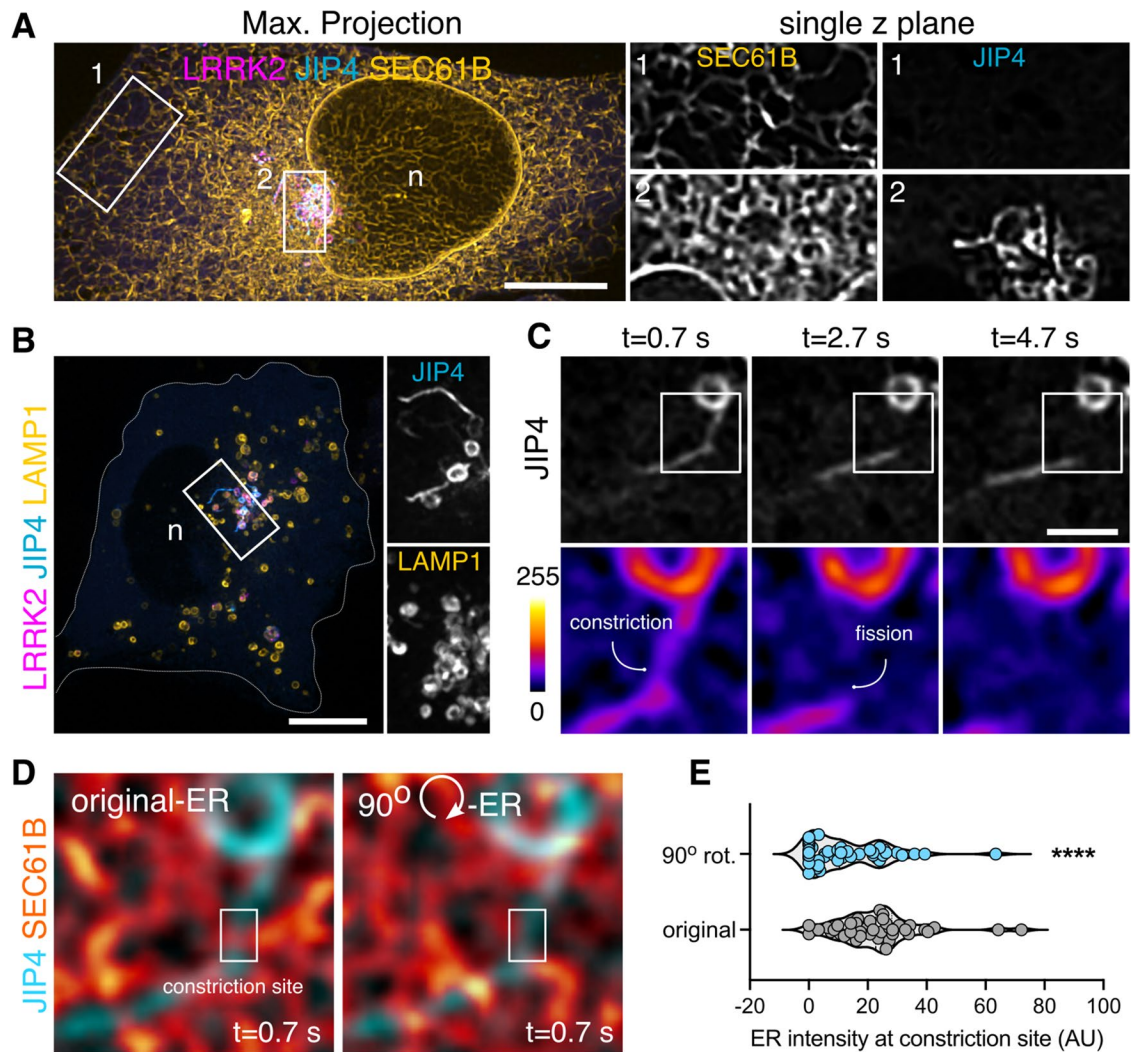
FIGURE 4: The presence of the ER in the constriction site is not a random event. (A) Cells were transfected with HaloTag-LRRK2 (magenta), mNeonGreen-JIP4 (cyan), and mCherry-SEC61B (yellow). After LLOMe treatment (1 mM, 2 h), cells were imaged under a confocal microscope. Representative confocal picture showing the cellular location of the JIP4-positive tubules in the context of the ER organization (n, nucleus). (B) Cells were transfected with HaloTag-LRRK2 (magenta), mNeonGreen-JIP4 (cyan), and LAMP1-RFP (yellow). After LLOMe treatment (1 mM, 2 h), cells were imaged under a confocal microscope. Representative confocal picture showing the perinuclear location of the JIP4-positive tubules and lysosomes. (C) Cells were transfected with 3xFLAG-LRRK2, mNeonGreen-JIP4 (gray and "Fire" LUT), and mNeonGreen-SEC61B. After LLOMe treatment (1 mM, 2 h), cells were imaged under a confocal microscope. Time-lapse imaging shows a sorting event. (D) Representative confocal pictures of the sorting event in C rotating the ER 90° to the right or not. (E) Violin plot shows the intensity of the ER in the constriction site, rotating the ER 90° to the right or not. Paired t test was applied ($p < 0.0001$, $n = 44$ cells measured). Data are depicted in a violin plot showing all points. Pictures in C and D are shown in one single z plane. Scale bar (A, B) = 10 µm; (C) = 2 µm.

intensity in the constriction site in the randomized group compared with the original group (Figure 4, D and E), indicating that the presence of the ER at the constriction site is not a random event.

The morphology of the ER regulates lysosomal membrane sorting

The ER exists in multiple morphological domains consisting of flat cisternae (also known as sheets) and tubules (Figure 5A) (Shibata et al., 2010; Nixon-Abell et al., 2016). ER tubules appear to be more dynamic than sheets (Figure 5B; Supplemental Movie 5) and often mark sites for mitochondrial division (Friedman et al., 2011), endosomal sorting (Rowland et al., 2014; Hoyer et al., 2018), and RNA granule division (Lee et al., 2020). Consequently, changes in the ER

morphology have been associated with decreased mitochondrial division (Adachi et al., 2020), endosomal sorting (Rowland et al., 2014), and RNA granule division (Lee et al., 2020). ER morphology is controlled by a conserved group of proteins. Reticulons and REEPs are required to generate tubules, while sheet formation is stimulated by Climp63, KTN1, or RRBP1 (for a review, see Wang and Rapoport, 2019) (Figure 5C). Climp63 is an ER transmembrane protein with a coiled-coil domain in the ER lumen (Shibata et al., 2010), and overexpression of Climp63 dramatically changes ER morphology, increasing the amount of sheets (Shibata et al., 2010; Gao et al., 2019; Lee et al., 2020) (Figure 5D). Thus. to ascertain whether the ER morphology plays a role in lysosomal tubule sorting, we overexpressed a tagged version of Climp63 (Figure 5D). Climp63 overexpression
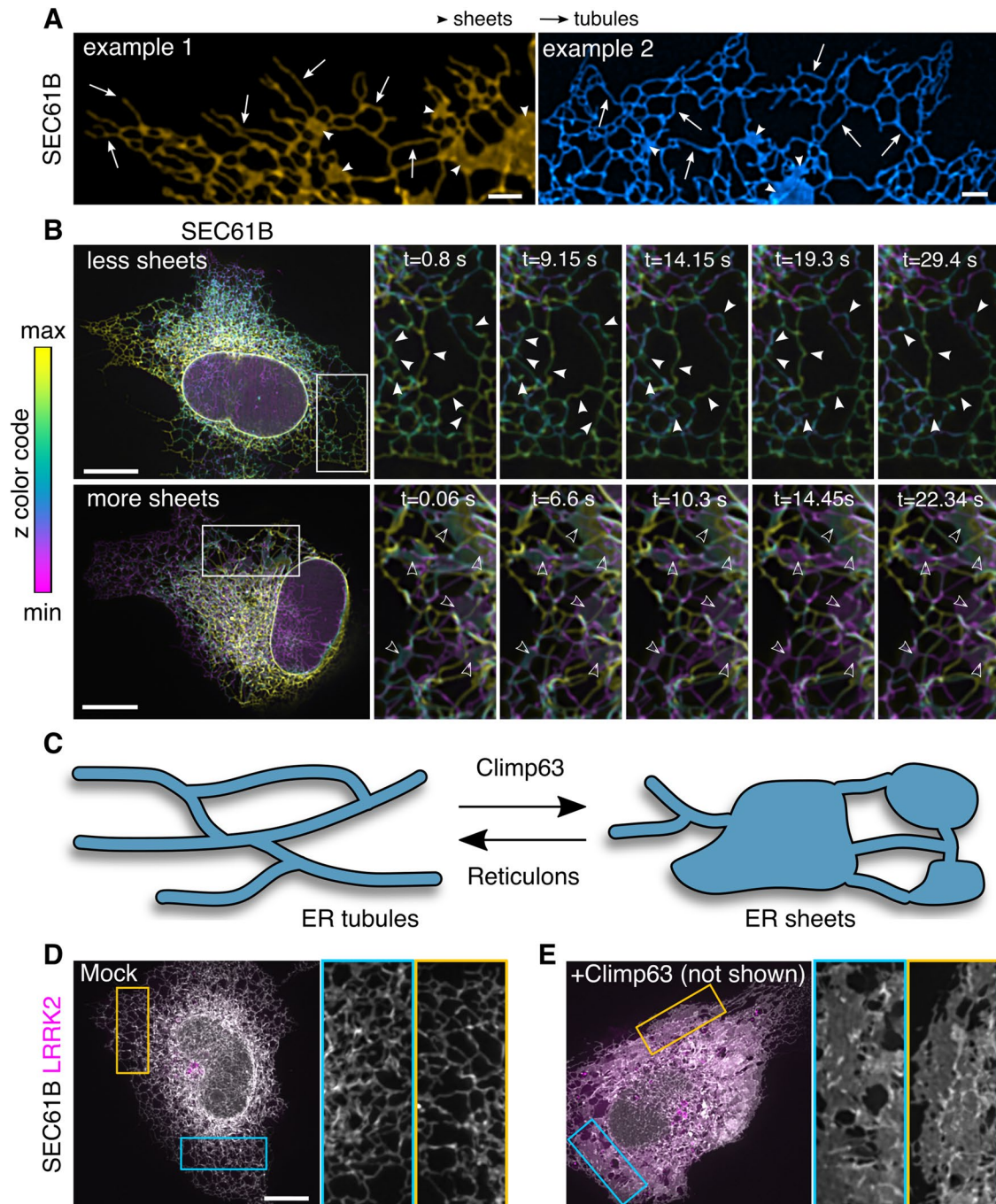
FIGURE 5: Climp63 overexpression alters the ER morphology by decreasing ER tubules and promoting ER sheets. (A, B) U2OS cells were transfected with HaloTag-SEC61B (yellow, cyan) and imaged live with a confocal microscope. (A) Arrowheads show ER sheets, while arrows show ER tubules. (B) Time-lapse images showing ER tubules (white arrowheads) and ER sheets (outlined arrowheads) displaying different dynamics over time. (C) Cartoon explaining the effect of Climp63 on ER morphology. (D, E) U2OS cells were transfected with HaloTag-LRRK2 (magenta) and mNeonGreen-SEC61B with (E) or without (D) mCherry-Climp63. Scale bar (A) = 2 μm; (B, D, E) = 10 μm.

(Climp63-OE) did not change the length of the JIP4-positive tubules (Figure 6, A and B) and leads to a marginal increase in the tubular ratio, which measures the number of JIP4-positive tubules divided by the number of JIP4-positive lysosomes in each cell (Figure 6, C and D). However, when the tubules were tracked using time-lapse microscopy, we observed a statistically significant decrease in the frequency of membrane sorting in the Climp63-OE cells compared with the Mock group (Figure 6, E and F; Supplemental Movie 6).

We also considered whether the PD protein VPS13C (Lesage et al., 2016; Nalls et al., 2019), a lipid transporter that tethers the ER to lysosomes (Kumar et al., 2018; Cai et al., 2022), could be involved in LYTL. We found VPS13C decorating vesicular structures distributed throughout the cytosol (Supplemental Figure S6A). VPS13C structures partially colocalize with LAMP1 but are LRRK2-negative (Supplemental Figure S6A). Interestingly, we observed that VPS13C can form tubules that are negative for LAMP1 (Supplemental Figure S6A)
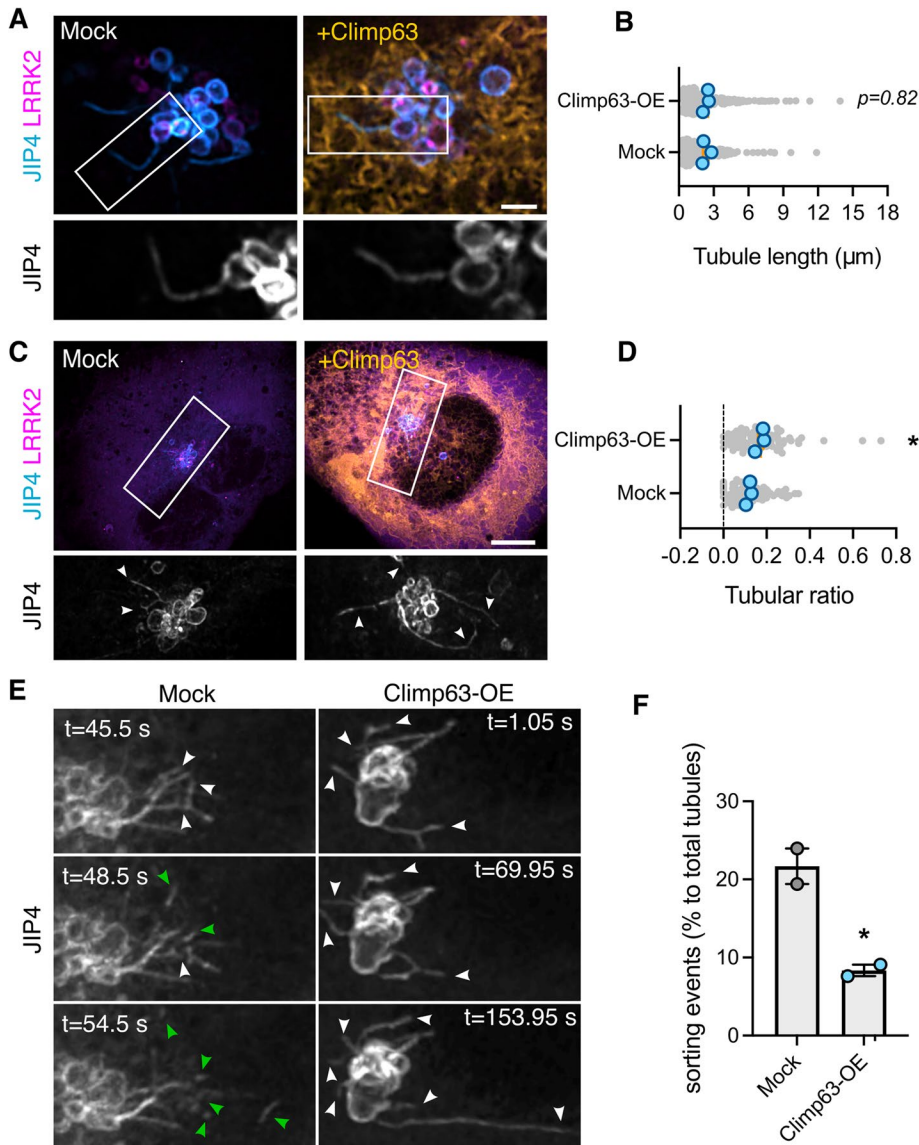
FIGURE 6: Redirecting ER tubules to ER sheets reduces lysosomal sorting. (A–D) U2OS cells were transfected with HaloTag-LRRK2 (magenta) and mNeonGreen-JIP4 (cyan, gray), with or without mCherry-Climp63 (yellow). Cells were treated with LLOMe (1 mM) for 2 h and analyzed under a confocal microscope. (A) Representative pictures of the JIP4 tubule length in mock cells and cells transfected with Climp63. (B) Graph showing the tubule length in both groups. Unpaired t test was applied ($p = 0.8227$, $n = 209$–298 total tubules analyzed respectively across three biological replicates). Data are means ± SEM. (C) Representative pictures of the tubular ratio in Mock cells and cells transfected with Climp63. (D) Graph showing the tubular ratio in both groups. An unpaired t test was applied ($p = 0.0249$, $n = 72$–74 cells analyzed respectively from three biological replicates). Data are means ± SEM. (E) Cells were transfected with 3xFLAG-LRRK2 and mNeonGreen-JIP4, with or without mCherry-Climp63. After treatment with LLOMe (1 mM, 2 h), cells were analyzed under a confocal microscope. Time-lapse images show tubule fission in Mock cells and cells transfected with mCherry-Climp63. (F) Histogram depicting the percentage of sorted tubules in two independent replicates. An unpaired t test was used for statistical inferences ($p = 0.0306$). Data are means ± SEM. White arrowheads show lysosomal tubules and green arrowheads signal tubules that undergo fission. Scale bar (A) = 2 μm; (B) = 10 μm.

even when they emanate from LAMP1-positive compartments (Supplemental Figure S6B). JIP4 is also absent from the VPS13C tubules, and VPS13C does not colocalize with the LYTL tubules (Supplemental Figure S6C). As VPS13C and LRRK2 are involved in familial and sporadic PD, it is possible that membrane tubulation plays an important role in PD pathogenesis. However, these results demonstrate that

VPS13C and LRRK2 tubules are distinct from each other and indicate that VPS13C is not a contributor to LYTL.

DISCUSSION

Lysosomes can remodel their membrane as an adaptive mechanism in response to multiple stimuli (for reviews, see Saffi and Botelho, 2019; Zoncu and Perera, 2022). For example, lysosomes can become tubulated in immune cells under inflammation conditions to deliver MHC-II: peptide complexes for antigen presentation (Chow et al., 2002; Saric et al., 2016). Lysosomes can also generate new lysosomes via lysosomal reformation (LR) to replenish the lysosomal pool during starvation (Yu et al., 2010) or after endocytosis (Bright et al., 2016). Lysosomes also remodel their membrane under conditions where damage is established. When cells are treated with lysosomotropic reagents to induce lysosomal membrane damage, lysosomes initiate membrane repair through ESCRT (Radulovic et al., 2018; Skowyra et al., 2018). If the damage persists, ruptured lysosomes are cleared through lysophagy (Maejima et al., 2013) to prevent lysosome-dependent cell death (Wang et al., 2018).

We have recently expanded the repertoire of lysosomal tubulation events by showing that lysosomes respond to membrane damage by LYTL (Bonet-Ponce et al., 2020). LYTL is initiated by lysosomal membrane damage and is then driven by the PD protein LRRK2. After being recruited to the lysosomal membrane, LRRK2 then phosphorylates the small GTPase RAB10, leading to accumulation of pRAB10 in the lysosomal membrane. As a result, pRAB10 recruits its effector JIP4 to LRRK2-positive lysosomes, likely through its RILP homology domain 2 (Waschbüsch et al., 2020). We have previously shown that LYTL tubules align with microtubules in cells, suggesting that the extrusion of the lysosomal membrane requires a motive force from microtubule-dependent transport via JIP4 as an adaptor protein, which needs to be confirmed in future studies. Although currently unknown, future work should be directed to addressing the role of LYTL in the general biology of the lysosome. For instance, it is possible that membrane sorting can alleviate lysosomal membrane damage and act as a protective response. Alternatively, the sorted vesicles could be secreted, acting as an intercellular communication system. LYTL tubules are consistently negative for all lysosomal membrane markers that we have analyzed (LAMP1, LAMP2, TMEM192, LAMTOR4, ARL8B, and LIMP2) in fixed or live cells, suggesting a retention mechanism to segregate these proteins away from the tubule membrane before elongation. This observation indicates that LYTL is distinct from LR where lysosomal membrane markers do end up in

FIGURE 7: Schematic representation of our working model. LRRK2 is recruited to ruptured lysosomes, where it phosphorylates and recruits RAB10. pRAB10 recruits its effector JIP4 that recruits an unknown motor protein to the lysosomal membrane. The LYTL tubules fission process is facilitated by the ER.

tubules. A limitation in our current understanding of LYTL is the lack of identified cargo sorted with the lysosomal-derived vesicles.

The ER establishes contacts with multiple cellular structures (Valm *et al.*, 2017; Wu *et al.*, 2018), which can consequently derive in promoting fission/division. We observe a clear contact of the ER with the JIP4-positive tubules, although not all LYTL tubules contact the ER (~60%), distinct from the reported 80 and 93% in early and late endosomes, respectively (Rowland *et al.*, 2014). One possible factor contributing to the differences in ER contact frequency between LYTL and other ER:organelle contact sites relates to cellular localization. ER-dependent fission events are usually studied in the cell periphery, where the ER forms a clear monolayer. In contrast, JIP4-positive tubules are located in the perinuclear area (Kluss *et al.*, 2020), where the ER is densely packed. Thus, ER tubules may have different properties depending on cellular location. Even though Climp63 overexpression reduces ER tubules and LYTL sorting, we cannot rule out the possibility of a direct role of Climp63 protein expression over LYTL sorting, rather than an effect of ER morphology itself. Thus, our data further emphasize the novel nature of LYTL and highlight its difference from other known fission/sorting processes. It will be interesting to study the fission process further and to uncover other players contributing to lysosomal membrane sorting and understand how/whether the ER tethers with the JIP4-positive tubules.

In summary here we have explored lysosomal tubulation and membrane sorting in living cells, allowing for dynamic imaging at high resolution. We describe new regulatory elements of LYTL, which is likely pathologically relevant given the role of LRRK2 and lysosomes in neurodegeneration. We demonstrate that LYTL sorting is distinct from other organellar fission events and is at least partially regulated by the ER (Figure 7).

MATERIALS AND METHODS
Request a protocol through *Bio-protocol*.

Cell culture
U2OS cells (American Type Culture Collection) and mouse primary astrocytes were maintained in DMEM (Thermo Fisher Scientific) containing 4.5 g/l glucose, 2 mM L-glutamine, and 10% fetal bovine serum (FBS) (Lonza) at 37°C in 5% CO_2 in 75 cm^2 tissue culture flasks. U2OS cells were used until passage 30. Cells were seeded on 12 mm coverslips for fixed experiments and in 35 mm glass bottom dishes (MatTek) for live-cell imaging experiments. Coverslips and dishes were precoated with Matrigel.

Primary astrocyte cultures were prepared from C57BL/6J newborn (postnatal day 0) pups. Dissected mouse cortices were incubated in 1 ml/cortex Basal medium Eagle (BME) (Sigma-Aldrich) containing 5 U of papain (Worthington) for 30 min at 37°C. Five micrograms of deoxyribonuclease I was added to each cortex preparation, and brain tissue was dissociated into a cellular suspension that was washed twice with 10 volumes of BME and cells were counted. Astrocyte cultures were plated in DMEM nutrient mixture F-12 (DMEM/F12) (Thermo Fisher Scientific), supplemented with 10% FBS (Lonza) in 75-cm^2 tissue culture flasks. For the preparation of purified astrocyte cultures, 7- to 10-d primary cultures were vigorously shaken to detach microglia and oligodendrocytes. Culture purity was assessed with GFAP for astrocytes and MAP2, OLIG2, and IBA1 to exclude neurons, oligodendrocytes, and microglia, respectively. Cultures had >90% of astrocytes in all experiments. Astrocytes were used from passage 2 to passage 3.

Plasmids
Constructs for 3xFLAG-LRRK2 and mNeonGreen-JIP4 have been described previously (Beilina *et al.*, 2014, 2020; Bonet-Ponce *et al.*, 2020). JIP4, LRRK2, and CORO1C cDNAs were amplified with PCR and cloned into the pCR8/GW/TOPO vector (Thermo Fisher Scientific). Each was then subcloned into pDEST vectors using Gateway technology (Thermo Fisher Scientific). LRRK2 was subcloned into the pDEST-HaloTag and pDEST-mScarlet vectors; JIP4 was subcloned into pDEST-HaloTag and pDEST-SNAPtag, and CORO1C was subcloned into pDEST-HaloTag.

LAMP1-RFP, LAMP1-mNeonGreen, mCherry-SEC61B, mCherry-Climp63, and TMEM192-3xHA plasmids were purchased from Addgene (Addgene#1817, #98882, #90994, #136293, and #102930) (Sherer *et al.*, 2003; Shibata *et al.*, 2008; Nixon-Abell *et al.*, 2016; Abu-Remaileh *et al.*, 2017; Chertkova *et al.*, 2017).

mNeonGreen-SEC61B and HaloTag-SEC61B were cloned by using the mCherry-SEC61B plasmid obtained from Addgene and replacing the tags using IN-FUSION. The LAMP1-HaloTag, ARL8B-mCherry, and VPS13C-HaloTag plasmids were gifts from Juan Bonifcacino (National Institutes of Health) and Pietro De Camilli (Yale University), respectively. All expression constructs used in this study are summarized in Supplemental Table 1.

Transfection
Transient transfections of U2OS and mouse primary astrocyte cells were performed using the Lipofectamine Stem Reagent and Opti-MEM (Thermo Fisher Scientific). U2OS cells were transfected for 36–48 h before imaging. Astrocytes were transfected for 48 h before imaging.

Confocal microscopy
Airyscan. Airyscan images were taken using a Zeiss LSM 880 microscope equipped with a 63× 1.4 NA objective. Superresolution imaging was performed using the Airyscan mode. Raw data were processed using Airyscan processing in "auto strength" mode with Zen Black software version 2.3.

SoRa. For spinning-disk superresolution microscopy we used a W1-SoRa superresolution spinning-disk microscope (Nikon) with a

60× 1.49 NA oil immersion objective. A 2.8× intermediate magnification (168× combined) was used in time-lapse experiments regarding JIP4 tubules. A 4× intermediate magnification (240× combined) was used in snapshot images and time-lapse images in Figure 5B. An offset microlensed SoRa disk was used with an environmental chamber to maintain cells at 37°C with humidified 5% CO_2 gas during imaging. For deconvolution, we used 10–25 iterations of the 3D Landweber algorithm with NIS-Elements AR 5.21.03 software. Images from two channels were acquired simultaneously using a Cairn twin-cam emission splitter and two Photometrics prime 95b sCMOS cameras, a 565LP DM, and appropriate emission cleanup filters. Triggered piezo was used to maximize speed. Stacks were taken with 0.2 µm distance between slices.

When needed, bleaching was corrected using the "Histogram matching" option from Fiji (ImageJ). Unless otherwise stated, stacks were processed as maximum intensity projection.

Lookup tables (LUTs)
All pseudocolors used in this paper can be found in the "NeuroCyto LUTs" collection (Fiji; ImageJ). For gray colors, "CET-L1" and "JDM grays g = 1.50" were used. For cyan colors, "cyan," "cyan hot," and "JDM04 pop cyan" were used. For magenta, "Magenta" and "Magenta Hot" were used. For orange, "NanoJ-Orange" was used. For yellow, "Yellow Hot" was used. To show fluorescence intensity in Figure 4C and Supplemental Figure S4, the "Fire" LUT was used. For z color code in Figure 5B, the "Z-stack Depth Colorcode 0.0.2" plug-in (Fiji; ImageJ) was applied using "DavLUT-Bright" as LUT.

Volume view
The volume view in Figure 1, C–G, was obtained using NIS-Elements AR 5.21.03 software (Nikon) with the "Alpha Blending" option with or without "Depth Color Code."

Tubular ratio measurements
U2OS cells were transfected with the 3xFLAG-LRRK2 plasmid and cotransfected with mNeonGreen-JIP4. After treatment with LLOMe, live cells were imaged with SorA. The tubular ratio in each cell was measured as Ratio = #JIP4 + tubules/#JIP4 + lysosomes. Only cells with 10 or more JIP4-positive lysosomes per cell were imaged.

ER presence in constriction site
Cells were transfected with the 3xFLAG-LRRK2, HaloTag-JIP4, and mNeonGreen-SEC61B plasmids. Forty-eight hours later, cells were treated with LLOMe for 2 h and tracked under the confocal microscope. Forty-four sorting events were detected, and the frame before the membrane fission was examined. The ER was kept in its original orientation and also rotated 90° to the right to randomize its position. The ER channel was thresholded in both cases, and a region of interest was drawn in the constriction site. The fluorescence intensity in both ER groups was measured and compared using a paired *t* test. Two- to four-minute movies were taken with a 2–4 s frame difference. Cells were imaged with the Dual Camera option to acquire both channels (JIP4 and SEC61B) simultaneously.

Immunostaining
Cells were fixed with 4% paraformaldehyde for 10 min, permeabilized with phosphate-buffered saline (PBS)/0.1% Triton for 10 min, and blocked with 5% donkey serum for 1 h at room temperature (RT). Primary antibodies were diluted in blocking buffer (1% donkey serum) and incubated overnight at 4°C. After three 5 min washes with PBS/0.1% Triton, secondary fluorescently labeled antibodies were diluted in blocking buffer (1% donkey serum) and incubated

for 1 h at RT. Coverslips were washed twice with 1× PBS and an additional two times with dH_2O and mounted with ProLong Gold antifade reagent (Thermo Fisher Scientific).

Statistical analysis
Statistical analysis for experiments with two treatment groups used Student's *t* tests with Welch's correction for unequal variance. An *F* test was used to assess the equality of variances of the *t* test. Unless otherwise stated, graphed data are presented as means ± SEM or violin plots. Comparisons that were considered statistically significant are indicated; *, $p < 0.05$; **, $p < 0.01$; ***, $p < 0.001$; ****, $p < 0.0001$.

REFERENCES
Abu-Remaileh M, Wyant GA, Kim C, Laqtom NN, Abbasi M, Chan SH, Freinkman E, Sabatini DM (2017). Lysosomal metabolomics reveals V-ATPase- and mTOR-dependent regulation of amino acid efflux from lysosomes. Science 358, 807–813.

Adachi Y, Kato T, Yamada T, Murata D, Arai K, Stahelin RV, Chan DC, Iijima M, Sesaki H (2020). Drp1 tubulates the ER in a GTPase-independent manner. Mol Cell 80, 621–632.e6.

Araki K, Nagata K (2011). Protein folding and quality control in the ER. Cold Spring Harb Perspect Biol 3, a007526.

Azuma T, Kei T (2015). Super-resolution spinning-disk confocal microscopy using optical photon reassignment. Opt Express 23, 15003–15011.

Ballabio A, Bonifacino JS (2020). Lysosomes as dynamic regulators of cell and organismal homeostasis. Nat Rev Mol Cell Biol 21, 101–118.

Beilina A, Rudenko IN, Kaganovich A, Civiero L, Chau H, Kalia SK, Kalia LV, Lobbestael E, Chia R, Ndukwe K, *et al.* (2014). Unbiased screen for interactors of leucine-rich repeat kinase 2 supports a common pathway for sporadic and familial Parkinson disease. Proc Natl Acad Sci USA 111, 2626–2631.

Beilina A, Bonet-Ponce L, Kumaran R, Kordich JJ, Ishida M, Mamais A, Kaganovich A, Saez-Atienzar S, Gershlick DC, Roosen DA, *et al.* (2020). The Parkinson's disease protein LRRK2 interacts with the GARP complex to promote retrograde transport to the trans-Golgi network. Cell Rep 31, 107614.

Bonet-Ponce L, Beilina A, Williamson CD, Lindberg E, Kluss JH, Saez-Atienzar S, Landeck N, Kumaran R, Mamais A, Bleck CKE, *et al.* (2020). LRRK2 mediates tubulation and vesicle sorting from lysosomes. Sci Adv 6, eabb2454.

Bonet-Ponce L, Cookson MR (2019). The role of Rab GTPases in the pathobiology of Parkinson' disease. Curr Opin Cell Biol 59, 73–80.

Bonet-Ponce L, Cookson MR (2021). LRRK2 recruitment, activity, and function in organelles. FEBS J, doi: 10.1111/febs.16099.

Bright NA, Davis LJ, Luzio JP (2016). Endolysosomes are the principal intracellular sites of acid hydrolase activity. Curr Biol 26, 2233–2245.

Cai S, Wu Y, Guillen-Samander A, Hancock-Cerutti WF, Liu J, De Camilli P (2022). In situ architecture of the lipid transport protein VPS13C at ER-lysosomes membrane contacts. Proc Natl Acad Sci USA 119, e2203769119.

Chauhan S, Kumar S, Jain A, Ponpuak M, Mudd MH, Kimura T, Choi SW, Peters R, Mandell M, Bruun JA, *et al.* (2016). TRIMs and galectins globally cooperate and TRIM16 and galectin-3 co-direct autophagy in endomembrane damage homeostasis. Dev Cell 39, 13–27.

Chertkova AO, Mastop M, Postma M, van Bommel N, van der Niet S, Batenburg KL, Joosen L, Gadella TWJ Jr, Okada Y, Goedhart J (2017). Robust and bright genetically encoded fluorescent markers for highlighting structures and compartments in mammalian cells, bioRxiv, 160374.

Chow A, Toomre D, Garrett W, Mellman I (2002). Dendritic cell maturation triggers retrograde MHC class II transport from lysosomes to the plasma membrane. Nature 418, 988–994.

Chu B-B, Liao Y-C, Qi W, Xie C, Du X, Wang J, Yang H, Miao H-H, Li B-L, Song B-L (2021). Cholesterol transport through lysosome-peroxisome membrane contacts. Cell 184, 289.

Cookson MR (2010). The role of leucine-rich repeat kinase 2 (LRRK2) in Parkinson's disease. Nat Rev Neurosci 11, 791–797.

Eapen VV, Swarup S, Hoyer MJ, Paulo JA, Harper JW (2021). Quantitative proteomics reveals the selectivity of ubiquitin-binding autophagy receptors in the turnover of damaged lysosomes by lysophagy. eLife 10, e72328.

Friedman JR, Lackner LL, West M, DiBenedetto JR, Nunnari J, Voeltz GK (2011). ER tubules mark sites of mitochondrial division. Science 334, 358–362.

Gao G, Zhu C, Liu E, Nabi IR (2019). Reticulon and CLIMP-63 regulate nanodomain organization of peripheral ER tubules. PLoS Biol 17, e3000355.

Goo MS, Sancho L, Slepak N, Boassa D, Deerinck TJ, Ellisman MH, Bloodgood BL, Patrick GN (2017). Activity-dependent trafficking of lysosomes in dendrites and dendritic spines. J Cell Biol 216, 2499–2513.

Guo Y, Li D, Zhang S, Yang Y, Liu JJ, Wang X, Liu C, Milkie DE, Moore RP, Tulu US, et al. (2018). Visualizing intracellular organelle and cytoskeletal interactions at nanoscale resolution on millisecond timescales. Cell 175, 1430–1442.e17.

Höglinger D, Burgoyne T, Sanchez-Heras E, Hartwig P, Colaco A, Newton J, Futter CE, Spiegel S, Platt FM, Eden ER (2019). NPC1 regulates ER contacts with endocytic organelles to mediate cholesterol egress. Nat Commun 10, 4276.

Hoyer MJ, Chitwood PJ, Ebmeier CC, Striepen JF, Qi RZ, Old WM, Voeltz GK (2018). A novel class of ER membrane proteins regulates ER-associated endosome fission. Cell 175, 254–265.e14.

Jabbari E, Koga S, Valentino RR, Reynolds RH, Ferrari R, Tan MMX, Rowe JB, Dalgard CL, Scholz SW, Dickson DW, et al. (2021). Genetic determinants of survival in progressive supranuclear palsy: a genome-wide association study. Lancet Neurol 20, 107–116.

Jia J, Abudu YP, Claude-Taupin A, Gu Y, Kumar S, Choi SW, Peters R, Mudd MH, Allers L, Salemi M, et al. (2018). Galectins control mTOR in response to endomembrane damage. Mol Cell 70, 120–135.e8.

Jia J, Claude-Taupin A, Gu Y, Choi SW, Peters R, Bissa B, Mudd MH, Allers L, Pallikkuth S, Lidke KA, et al. (2020). Galectin-3 coordinates a cellular system for lysosomal repair and removal. Dev Cell 52, 69–87.e8.

Klein AD, Mazzulli JR (2018). Is Parkinson's disease a lysosomal disorder? Brain 141, 2255–2262.

Kluss JH, Beilina A, Williamson CD, Lewis PA, Cookson MR, Bonet-Ponce L (2020). Lysosomal positioning regulates Rab10 phosphorylation at LRRK2-positive lysosomes, bioRxiv, 406223.

Kluss JH, Bonet-Ponce L, Lewis PA, Cookson MR (2022). Directing LRRK2 to membranes of the endolysosomal pathway triggers RAB phosphorylation and JIP4 recruitment. Neurobiol Dis 170, 105769.

Kumar N, Leonzino M, Hancock-Cerutti W, Horenkamp FA, Li P, Lees JA, Wheeler H, Reinisch KM, De Camilli P (2018). VPS13A and VPS13C are lipid transport proteins differentially localized at ER contact sites. J Cell Biol 217, 3625–3639.

Lee JE, Cathey PI, Wu H, Parker R, Voeltz GK (2020). Endoplasmic reticulum contact sites regulate the dynamics of membraneless organelles. Science 367, eaay7108.

Lesage S, Drouet V, Majounie E, Deramecourt V, Jacoupy M, Nicolas A, Cormier-Dequaire F, Hassoun SM, Pujol C, Ciura S, et al. (2016). Loss of VPS13C function in autosomal-recessive parkinsonism causes mitochondrial dysfunction and increases PINK1/Parkin-dependent mitophagy. Am J Hum Genet 98, 500–513.

Liao YC, Fernandopulle MS, Wang G, Choi H, Hao L, Drerup CM, Patel R, Qamar S, Nixon-Abell J, Shen Y, et al. (2019). RNA granules hitchhike on lysosomes for long-distance transport, using annexin A11 as a molecular tether. Cell 179, 147–164.e20.

Lim C-Y, Davis OB, Shin HR, Zhang J, Berdan CA, Jiang X, Counihan JL, Ory DS, Nomura DK, Zoncu R (2019). ER-lysosome contacts enable cholesterol sensing by mTORC1 and drive aberrant growth signalling in Niemann-Pick type C. Nat Cell Biol 21, 1206–1218.

Maejima I, Takahashi A, Omori H, Kimura T, Takabatake Y, Saitoh T, Yamamoto A, Hamasaki M, Noda T, Isaka Y, et al. (2013). Autophagy sequesters damaged lysosomes to control lysosomal biogenesis and kidney injury. EMBO J 32, 2336–2347.

Meng Y, Heybrock S, Neculai D, Saftig P (2020). Cholesterol handling in lysosomes and beyond. Trends Cell Biol 30, 452–466.

Nalls MA, Blauwendraat C, Vallerga CL, Heilbron K, Bandres-Ciga S, Chang D, Tan M, Kia DA, Noyce AJ, Xue A, et al. (2019). Identification of novel risk loci, causal insights, and heritable risk for Parkinson's disease: a meta-analysis of genome-wide association studies. Lancet Neurol 18, 1091–1102.

Nixon-Abell J, Obara CJ, Weigel AV, Li D, Legant WR, Xu CS, Pasolli HA, Harvey K, Hess HF, Betzig E, et al. (2016). Increased spatiotemporal resolution reveals highly dynamic dense tubular matrices in the peripheral ER. Science 354, aaf3928.

Padamsey Z, McGuinness L, Bardo SJ, Reinhart M, Tong R, Hedegaard A, Hart ML, Emptage NJ (2017). Activity-dependent exocytosis of lysosomes regulates the structural plasticity of dendritic spines. Neuron 93, 132–146.

Paisán-Ruíz C, Jain S, Evans EW, Gilks WP, Simón J, van der Brug M, López de Munain A, Aparicio S, Gil AM, Khan N, et al. (2004). Cloning of the gene containing mutations that cause PARK8-linked Parkinson's disease. Neuron 44, 595–600.

Radulovic M, Schink KO, Wenzel EM, Nähse V, Bongiovanni A, Lafont F, Stenmark H (2018). ESCRT-mediated lysosome repair precedes lysophagy and promotes cell survival. EMBO J 37, e99753.

Rowland AA, Chitwood PJ, Phillips MJ, Voeltz GK (2014). ER contact sites define the position and timing of endosome fission. Cell 159, 1027–1041.

Saffi GT, Botelho RJ (2019). Lysosome fission: planning for an exit. Trends Cell Biol 29, 635–646.

Saric A, Hipolito VEB, Kay JG, Canton J, Antonescu CN, Botelho RJ (2016). mTOR controls lysosome tubulation and antigen presentation in macrophages and dendritic cells. Mol Biol Cell 27, 321–333.

Sherer NM, Lehmann MJ, Jimenez-Soto LF, Ingmundson A, Horner SM, Cicchetti G, Allen PG, Pypaert M, Cunningham JM, Mothes W (2003). Visualization of retroviral replication in living cells reveals budding into multivesicular bodies. Traffic 4, 785–801.

Shibata Y, Shemesh T, Prinz WA, Palazzo AF, Kozlov MM, Rapoport TA (2010). Mechanisms determining the morphology of the peripheral ER. Cell 143, 774–788.

Shibata Y, Voss C, Rist JM, Hu J, Rapoport TA, Prinz WA, Voeltz GK (2008). The reticulon and DP1/Yop1p proteins form immobile oligomers in the tubular endoplasmic reticulum. J Biol Chem 283, 18892–18904.

Skowyra ML, Schlesinger PH, Naismith TV, Hanson PI (2018). Triggered recruitment of ESCRT machinery promotes endolysosomal repair. Science 360, eaar5078.

Spits M, Heesterbeek IT, Voortman LM, Akkermans JJ, Wijdeven RH, Cabukusta B, Neefjes J (2021). Mobile late endosomes modulate peripheral endoplasmic reticulum network architecture. EMBO Rep 22, e50815.

Steger M, Tonelli F, Ito G, Davies P, Trost M, Vetter M, Wachter S, Lorentzen E, Duddy G, Wilson S, et al. (2016). Phosphoproteomics reveals that Parkinson's disease kinase LRRK2 regulates a subset of Rab GTPases. eLife 5, e12813.

Udayar V, Chen Y, Sidransky E, Jagasia R (2022). Lysosomal dysfunction in neurodegeneration: emerging concepts and methods. Trends Neurosci 45, 184–199.

Valm AM, Cohen S, Legant WR, Melunis J, Hershberg U, Wait E, Cohen AR, Davidson MW, Betzig E, Lippincott-Schwartz J (2017). Applying systems-level spectral imaging and analysis to reveal the organelle interactome. Nature 546, 162–167.

Wang F, Gómez-Sintes R, Boya P (2018). Lysosomal membrane permeabilization and cell death. Traffic 19, 918–931.

Wang N, Rapoport TA (2019). Reconstituting the reticular ER network—mechanistic implications and open questions. J Cell Sci 132, jcs227611.

Waschbüsch D, Purlyte E, Pal P, McGrath E, Alessi DR, Khan AR (2020). Structural basis for Rab8a recruitment of RILPL2 via LRRK2 phosphorylation of Switch 2. Structure 28, 406–417.e6.

Wong YC, Ysselstein D, Krainc D (2018). Mitochondria-lysosome contacts regulate mitochondrial fission via RAB7 GTP hydrolysis. Nature 554, 382–386.

Wu H, Carvalho P, Voeltz GK (2018). Here, there, and everywhere: the importance of ER membrane contact sites. Science 361, eaan5835.

Yu L, McPhee CK, Zheng L, Mardones GA, Rong Y, Peng J, Mi N, Zhao Y, Liu Z, Wan F, et al. (2010). Termination of autophagy and reformation of lysosomes regulated by mTOR. Nature 465, 942–946.

Zimprich A, Biskup S, Leitner P, Lichtner P, Farrer M, Lincoln S, Kachergus J, Hulihan M, Uitti RJ, Calne DB, et al. (2004). Mutations in LRRK2 cause autosomal-dominant parkinsonism with pleomorphic pathology. Neuron 44, 601–607.

Zoncu R, Perera RM (2022). Built to last: lysosome remodeling and repair in health and disease. Trends Cell Biol 32, 597–610.